RESEARCH ARTICLE | DECEMBER 16 2024

Nuclear quantum effects on glassy water *under* pressure: Vitrification and pressure-induced transformations

Special Collection: JCP and CPR Editors' Choice 2024

Ali Eltareb ; Bibi A. Khan ; Gustavo E. Lopez ; Nicolas Giovambattista

J. Chem. Phys. 161, 234502 (2024)
https://doi.org/10.1063/5.0238823
CHORUS

The Journal of Chemical Physics ARTICLE pubs.aip.org/aip/jcp

Nuclear quantum effects on glassy water *under* pressure: Vitrification and pressure-induced transformations

Cite as: J. Chem. Phys. 161, 234502 (2024); doi: 10.1063/5.0238823
Submitted: 14 September 2024 • Accepted: 15 November 2024 •
Published Online: 16 December 2024

Ali Eltareb,[1,2,a] Bibi A. Khan,[1,3,b] Gustavo E. Lopez,[3,4,c] and Nicolas Giovambattista[1,2,3,d]

AFFILIATIONS

[1] Department of Physics, Brooklyn College of the City University of New York, Brooklyn, New York 11210, USA
[2] Ph.D. Program in Physics, The Graduate Center of the City University of New York, New York, New York 10016, USA
[3] Ph.D. Program in Chemistry, The Graduate Center of the City University of New York, New York, New York 10016, USA
[4] Department of Chemistry, Lehman College of the City University of New York, Bronx, New York 10468, USA

[a] **Author to whom correspondence should be addressed:** aeltareb@gradcenter.cuny.edu
[b] bibi.khan2@lc.cuny.edu
[c] gustavo.lopez1@lehman.cuny.edu
[d] ngiovambattista@brooklyn.cuny.edu

ABSTRACT

We perform classical molecular dynamics (MD) and path-integral MD (PIMD) simulations of H_2O and D_2O using the q-TIP4P/F model over a wide range of temperatures and pressures to study the nuclear quantum effects (NQEs) on (i) the vitrification of liquid water upon isobaric cooling at different pressures and (ii) pressure-induced transformations at constant temperature between low-density amorphous and high-density amorphous ice (LDA and HDA) and hexagonal ice I_h and HDA. Upon isobaric cooling, classical and quantum H_2O and D_2O vitrify into a continuum of intermediate amorphous ices (IA), with densities in-between those of LDA and HDA (depending on pressure). Importantly, the density of the IA varies considerably if NQEs are included (similar conclusions hold for ice I_h at all pressures studied). While the structure of the IA is not very sensitive to NQE, the geometry of the hydrogen-bond (HB) is. NQE leads to longer and less linear HB in LDA, HDA, and ice I_h than found in the classical case. Interestingly, the delocalization of the H/D atoms is non-negligible and identical in LDA, HDA, and ice I_h at all pressures studied. Our isothermal compression/decompression MD/PIMD simulations show that classical and quantum H_2O and D_2O all exhibit LDA–HDA and ice I_h-HDA transformations, consistent with experiments. The inclusion of NQE leads to a softer HB-network, which lowers slightly the LDA/ice I_h-to-HDA transformation pressures. Interestingly, the HB in HDA is longer and less linear than in LDA, which is counterintuitive given that HDA is ≈25% denser than LDA. Overall, our results show that, while classical computer simulations provide the correct qualitative phenomenology of ice and glassy water, NQEs are necessary for a quantitative description.

I. INTRODUCTION

Water is one of the most complex substances on Earth, with its unique properties playing a fundamental role in numerous scientific and engineering applications.[1–3] For example, the phase diagram of water is particularly rich, with more than 19 crystalline forms.[4–8] At low temperatures, in the supercooled liquid state, water can exist in two different liquid states,[9,10] low-density and high-density liquid water (LDL and HDL). In the P–T plane, LDL and HDL are separated by a first-order liquid–liquid phase transition (LLPT) line that ends at a liquid–liquid critical point (LLCP) at approximately P_c = 50 – 250 MPa and T_c ≈ 170 – 220 K.[11–16] Relevant to this work is the complex phase behavior of glassy water (or amorphous ice). At approximately T < 140 K and P < 1000 MPa, water can exist in two different glassy states, low-density and high-density amorphous ice (LDA and HDA).[8,17–23] LDA can be formed by rapidly quenching

liquid water at atmospheric pressure[14,24] or by vapor deposition on a cold substrate.[25–32] Similarly, HDA can be obtained by cooling liquid water at high pressures[33] or by isothermal-compression of LDA[18,34–36] and hexagonal ice.[17,35,37–40] Numerous experiments indicate that LDA and HDA can be interconverted by isothermal compression–decompression at $T = 130$–140 K and isobaric heating at different pressures (see Refs. 14, 19, 35, 36, 39, and 41–43). The pressure-induced isothermal LDA–HDA transitions at $T \approx 130$–140 K are sharp and resemble a first-order phase transition with significant changes in the thermodynamic and structural properties (e.g., the difference in density between LDA and HDA is ~20%–25%). Indeed, in the LLPT scenario, LDA and HDA are the glassy counterparts of LDL and HDL. While other scenarios have been proposed to explain the anomalous behavior of liquid and glassy water, the LLPT scenario is currently the best explanation, supported by numerous computational,[44–55] experimental,[9,10,12,14,56–59] and theoretical studies.[15,60–65]

Numerous experimental and computational/theoretical studies have shed light on our understanding of the puzzling properties of LDA and HDA and their relationship to LDL and HDL.[4,9,10] Most computational studies of glassy water are based on classical molecular dynamics (MD) simulations employing rigid water models, such as ST2,[66–70] SPC/E,[71] and TIP4P/2005.[72–75] Recently, MD simulations of flexible water models[76] as well as coarse-grained water-like models[77,78] have also been applied to study glassy water. While these studies qualitatively reproduce the structural properties of LDA and HDA, as well as the transformation between LDA and HDA, they neglect the inclusion of atomic delocalization due to nuclear quantum effects (NQEs). We note that while classical rigid/flexible water models have been parameterized to match experimental properties, thereby incorporating NQE implicitly, they neglect atomic delocalization. Consequently, these models cannot be used in path-integral molecular dynamics (PIMD) simulations, as they would overestimate quantum effects since PIMD already includes NQE explicitly.[79] By the same token, classical MD simulations, based on any given water model, cannot be used to study isotope substitution effects, including the different behavior of H_2O and D_2O. This is important since experiments show that the physical and mechanical properties of H_2O and D_2O differ. For example, the glass transition temperature (T_g) of D_2O and H_2O differ by ~5 K, and the corresponding temperature of maximum density (T_{MD}) differs by about 8 K. We note that the vibrational frequency of the O–H stretching mode in H_2O is higher than the O–D stretching mode in D_2O, implying that the hydrogen atom oscillates faster than the deuterium atom. These faster oscillations can disrupt the hydrogen bond network of water, suggesting that D_2O forms stronger hydrogen bonds than H_2O. While some thermodynamic properties, such as the melting temperature of ice I_h, support the idea that D_2O forms stronger hydrogen bonds than H_2O, this may not hold true for all working conditions (e.g., temperatures and pressures).

Computer simulations show that NQEs are relevant in supercooled water, ice, and amorphous ice. NQEs affect the location of water's LLCP, as well as the thermodynamic properties of ice and LDA at normal pressure.[80–82] While the relevance of NQE in water at very high-pressures is well-supported by experiments,[83,84] the role of NQE on the phase behavior of glassy water and its relationship with ice remains poorly understood. In this work, we extend our previous path-integral molecular dynamics (PIMD) simulation study of LDA and ice I_h at $P = 0.1$ MPa[80] using the flexible q-TIP4P/F model. The q-TIP4P/F model incorporates intramolecular flexibility by modeling the O–H covalent bond with a quartic expansion of the Morse potential and a simple harmonic potential to model the potential energy of the HOH angle.[85] Additionally, the q-TIP4P/F model has been optimized for PIMD simulations and reproduces remarkably well the properties of liquid water,[44,85,86] ice I_h,[80,87,88] and LDA[76,80,81] at $P = 0.1$ MPa. We use the q-TIP4P/F model to investigate (i) the thermodynamic and structural properties of different amorphous ices produced by isobaric cooling at different pressures (vitrification) and (ii) the pressure induced LDA–HDA and ice I_h-HDA transformation at different temperatures. The aim of this study is to determine the role of NQE, due to the atoms delocalization in water, particularly the H/D atoms, on the thermodynamic and structural properties of LDA, ice I_h, and HDA. In addition, we also explore the effect of isotope substitution ($H_2O \rightarrow D_2O$) on the pressure-induced LDA–HDA and ice I_h-HDA transformations at $T = 80$ K. To our knowledge, this is the first time that the thermodynamic and structural properties of glassy water for D_2O are studied computationally using PIMD.

This work is organized as follows. In Sec. II, we present the computer simulation details. The results are presented in Sec. III and a summary is included in Sec. IV.

II. COMPUTER SIMULATIONS DETAILS

We perform out-of-equilibrium classical MD and PIMD simulations of H_2O and D_2O in the liquid, ice, and glassy state over a wide range of temperatures and pressures. Specifically, we focus on (i) isobaric cooling runs at different pressures to study the vitrification of liquid water under pressure, and (ii) isothermal compression/decompression runs at different temperatures to study the pressure-induced LDA–HDA and ice I_h-HDA transformations. (i) Isobaric cooling runs are performed at $P = 0.1, 100, 200, 400, 600, 800$, and 1000 MPa to generate amorphous ice that is directly related to the liquid state under pressure. As shown in Ref. 76 using classical MD simulations of q-TIP4P/F water, isobaric cooling of liquid water performed at $P = 0.1$ MPa generates LDA, while isobaric cooling of liquid water at high pressures $P \geq 400$ MPa produces HDA-like states. In these cooling MD/PIMD simulations, the liquid is equilibrated at $T = 240$ K and target P is cooled down to $T = 35$ K; the thermostat temperature is reduced linearly with time, using a cooling rate of $q_T = 10$ K/ns. We note that this cooling rate is ≈3 orders of magnitude faster than the experimental rate ≈0.01 K/ns[24,89] used to vitrify liquid water at $P = 0.1$ MPa. Nonetheless, the amorphous ices obtained at rate $q_T = 10$ K/ns are qualitatively similar to those found in experiments.[70,72,73,76–78,90–92]

(ii) In order to study the pressure induced LDA–HDA transformations at a given temperature T, we first compress the LDA obtained in (i) at $P = 0.1$ MPa and target T while keeping the thermostat temperature constant. During the isothermal compression, the barostat pressure is increased using a constant rate of $q_P = 100$ MPa/ns. This procedure transforms LDA into HDA at high pressures. The so obtained HDA is then decompressed at the same rate and temperature until the system fractures at very negative

pressure (tension). Compression/decompressions of LDA/HDA are performed at $T = 40, 60, 80, 100,$ and 120 K. Similar MD/PIMD simulations of H_2O and D_2O are performed starting from equilibrated hexagonal ice I_h configurations at $T = 50, 80, 150,$ and 200 K (and $q_P = 100$ MPa/ns). Compression of ice I_h also produces HDA.[17,37]

For comparison, we also perform equilibrium PIMD simulations of ice I_h for a system composed of $N = 1024$ molecules. These computer simulations are run over a wide range of temperatures, $25 \le T \le 300$ K, and pressures, $-1000 \le P \le 1000$ MPa. At a given T and P, the system is equilibrated for 0.5 ns, followed by a production run of 1.5 ns.

All our MD/PIMD simulations are based on the q-TIP4P/F model.[85] Isobaric cooling runs are for a system composed of $N = 512$ water molecules; compression/decompression runs to study the LDA–HDA and ice I_h-HDA transformation are for systems with $N = 512$ and $N = 1024$ water molecules, respectively. In our MD/PIMD simulations, the temperature is controlled using a stochastic (local) path-integral Langevin equation (PILE) thermostat,[93] while the pressure is maintained using a Monte Carlo (MC) barostat.[94,95] To control the temperature, the thermostat collision frequency parameter is set to $\gamma = 0.1$ ps^{-1}. To control the pressure, the frequency of the MC barostat is set to 25 simulation steps. In the PIMD simulations, the time step is $dt = 0.25$ fs and the number of beads per ring-polymer/atom is set to $n_b = 128$. As shown in Ref. 80, this value of n_b is large enough to obtain converged values for thermodynamic and structural properties of q-TIP4P/F water in the glass and ice I_h states at $P = 0.1$ MPa. Short-range (Lennard-Jones pair potential) interactions are calculated using a cutoff of $r_c = 1.0$ nm, and the long-range electrostatic interactions are computed using the reaction-field technique[96] with the same cutoff r_c. In the reaction-field calculation, the dielectric constant (relative permittivity) of the continuum medium beyond the cutoff radius r_c is set to 78.3. Classical MD simulations of ice I_h and LDA/HDA are also performed by setting $n_b = 1$ in the PIMD simulations. The same computational details described earlier hold for the classical MD simulations except that the time step is increased to $dt = 0.5$ fs. All of our MD/PIMD simulations are performed using the OpenMM (version 7.4.0) software package[97] and are based on a orthorhombic and cubic system for ice I_h and LDA/HDA, respectively, with periodic boundary conditions.

III. RESULTS

The results are presented as follows. In Sec. III A, we discuss the thermodynamic and structural properties of q-TIP4P/F water (H_2O) upon cooling at different pressures, from the liquid to the glass state, in the presence/absence of NQE. For comparison, we also discuss the properties of ice I_h at different pressures and temperatures. We show that isobaric cooling under pressure produces a continuum of amorphous ices and discuss the role of NQE on the density, radial distribution functions, hydrogen-bonding properties, and atom delocalization of glassy water. In Sec. III B, we discuss the role of NQE on the (i) pressure-induced LDA–HDA transformations and the (ii) compression-induced ice I_h-to-HDA transformation of water at different temperatures. Here, we focus on both H_2O and D_2O studied using PIMD and MD simulations and explore how the inclusion of NQE affects the hydrogen-bond network of H_2O/D_2O. An overview of the transformations between the glassy states of water and ice I_h for H_2O is summarized in Sec. IV, where an out-of-equilibrium phase diagram is included.

A. Nuclear quantum effects on amorphous ices produced by isobaric cooling under pressure

1. A continuum of amorphous ices

Figure 1(a) shows the density of q-TIP4P/F water (H_2O) during isobaric cooling at $P = 0.1, 100, 200, 400, 600, 800,$ and 1000 MPa

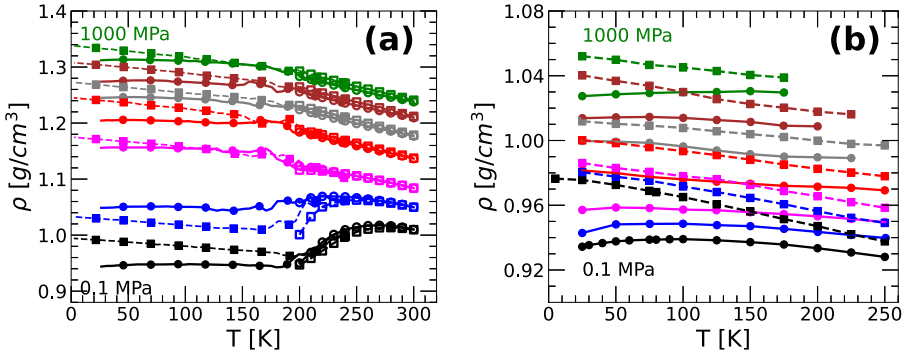

FIG. 1. (a) Density of q-TIP4P/F water as a function of temperature during vitrification at $P = 0.1, 100, 200, 400, 600, 800,$ and 1000 MPa (bottom-to-top). Solid and dashed lines represent the results from PIMD and classical MD simulations during the isobaric cooling, respectively. For clarity, we also plot solid circles and squares at every 25 K interval from the isobaric cooling, corresponding to the PIMD and classical MD simulations, respectively. Liquid water is first equilibrated at $T = 240$ K, and then it is cooled at constant pressure with a rate $q_T = 10$ K/ns; glassy water forms at approximately $T \approx 150$–180 K. Open circles and squares indicate the densities of equilibrium liquid water at $T \ge 200$ K obtained from PIMD and classical MD simulations, respectively. At all pressures studied, classical MD simulations predict that the density of glassy water increases linearly with T upon cooling while, instead, PIMD simulations (NQE included) show that the density of glassy remains constant or shows a very mild maxima upon cooling. (b) Density of q-TIP4P/F ice I_h as a function of temperature for the same pressures included in (a). Symbols and colors are the same as in (a) and (b), except in (b) the solid and dashed lines serve as a guide for the eye. NQE in ice I_h are pronounced at all pressures and temperatures; including NQE leads to lower densities, relative to the classical case, and a density maximum in ice I_h at low pressures (classical MD simulations show an increase in the density of ice I_h upon cooling).

from both classical MD (solid squares) and PIMD simulations (solid circles). At each pressure, the liquid is first equilibrated at $T = 240$ K, and then it is cooled down to $T \approx 35$ K into the glassy state using a cooling rate $q_T = 10$ K/ns. In addition, included in Fig. 1(a) are the equilibrium liquid densities of water at $T \geq 200$ K, obtained from classical MD (open squares) and PIMD simulations (open circles). In the classical case (MD simulations), the density of the liquid during the cooling process (solid squares) overlaps with the corresponding density of the equilibrated classical liquid (open squares). This holds down to $T' = 200$ K at high pressures ($P \geq 200$ MPa) and $T' = 200$–230 K at low pressures ($P = 0.1, 100$ MPa). Accordingly, T' indicates approximately the temperature at which the liquid departs from equilibrium during the cooling process. The same physical scenario holds if NQE are included (PIMD simulations; solid and empty circles). At most pressures considered, the values of T' obtained from classical MD and PIMD simulations are practically identical. Differences in T' occur at $P = 100$ MPa, close to the LLCP pressure of q-TIP4P/F water (see below).

Interestingly, NQE do not play a relevant role in the equilibrium liquid state at $T > T'$. At most of the pressures considered, the density of water at $T > T'$ obtained from classical MD and PIMD simulations practically overlap. Deviations between classical MD and PIMD simulations are observable at $P = 100$ MPa and $T = 200$–230 K (blue empty circles and squares). This is because, as discussed in detail in Ref. 44, the LLCP of q-TIP4P/F water (using the Reaction Field technique to treat the electrostatic interactions; this work) is located at $P_c \approx 135$ MPa and $T_c \approx 180$ K.[98] As shown in Ref. 44, introducing NQEs shifts the location of the LLCP in the P–T plane and, hence, NQE can affect the thermodynamic properties of water (e.g., density) at thermodynamic conditions close to the LLCP.

One of the main points of Fig. 1(a) is that NQE play an important role in the description of glassy water (at, safely, $T < 150$ K[80]). Specifically, except for the cooling run at $P = 100$ MPa, the densities of glassy water obtained from classical MD simulations are larger than those obtained from PIMD simulations by $\approx 0.02 - 0.05$ g/cm^3 at $T = 80$ K. The case of $P = 100$ MPa is complicated by the fact that this pressure is very close to the LLCP pressure of q-TIP4P/F water, and the location of the LLCP within the P–T plane varies slightly with the inclusion/exclusion of NQE. Hence, the critical fluctuations induced by the LLCP at $P = 100$ MPa may affect the classical/quantum q-TIP4P/F water to a different degree. As shown in Ref. 76, the critical density fluctuations induced by the LLCP in the liquid also produce dispersion in the density of the glass obtained upon cooling in independent runs (particularly for small systems composed of $N \approx 500$ as the system studied in this work). We also note that classical MD simulations predict that the density of glassy water increases upon cooling while, instead, PIMD simulations (NQE) show that the density of glassy water either saturates or exhibits a very mild maximum at low temperatures [see Ref. 80 for the detailed discussion of NQE on glassy water (LDA) at 0.1 MPa].

For comparison, we include in Fig. 1(b) the equilibrium densities of q-TIP4P/F ice I_h obtained from classical MD/PIMD simulations as a function of temperature and for the same pressures included in Fig. 1(a). As for the case of glassy water, classical MD simulations predict that the density of ice I_h increases upon cooling while, instead, PIMD simulations (NQE included) show that the density of ice I_h varies very weakly with temperature. At low pressures (approximately $P < 350$ MPa; see the supplementary material), the inclusion of NQE leads to a maximum in the density of ice I_h at low temperatures.[80–82,99–101] Including NQE (PIMD simulations) reduces the density of ice I_h by ~0.02–0.06 g/cm^3 at $T = 80$ K, relative to the classical case, which is similar to the differences seen in the glasses [see Fig. 1(a)]. Note that the experimental densities of ice I_h and glassy water (LDA) at $P = 0.1$ MPa are in agreement with our results based on PIMD simulations, indicating that NQE are necessary to study ice at low temperatures.[80–82,99,100]

As we will discuss below, while NQE are important to reproduce quantitatively the thermodynamic properties of glassy water,[80] both classical MD and PIMD simulations provide the same qualitative phase behavior of amorphous ice. In this regard, the results in Fig. 1 are particularly important. Consistent with Ref. 76, Fig. 1(a) shows that by appropriately selecting the pressure to vitrify water, it is possible to generate a continuum of amorphous ices with densities that lay in between the densities of LDA and HDA ($\rho_{LDA} \approx 0.94$ g/cm^3 and $\rho_{HDA} \approx 1.13$–1.17 g/cm^3 at $T = 80$ K); we will refer to the amorphous ices with intermediate densities ($\rho_{LDA} < \rho < \rho_{HDA}$) as intermediate amorphous ices (IA).[76] While both classical MD and PIMD both show that a continuum of IA can be produced by isobaric cooling at different pressures, the specific IA obtained in each case (at a given pressure) differ from one another. We note that Fig. 1(a) seems to suggest that there is a gap in the densities of the IA, between 1.05 and 1.15 g/cm^3. This is because Fig. 1(a) includes results from PIMD simulations at a few pressures, $P = 0.1, 100, 200, 400, 600, 800$, and 1000 MPa. As shown in Ref. 76, when more pressures are included, the density of the corresponding IA increases continuously with increasing cooling pressure.

In Ref. 76, it is shown that the density and structure of the IA obtained in classical MD simulations by isobaric cooling at $P = 125$ MPa is remarkably similar to the density and structure of the recently discovered medium-density amorphous (MDA);[4] similar results were found in Ref. 78 for a machine-learning coarse grained water-like model. For example, the density of the so obtained IA at $T = 80$ K is $\rho = 1.07$ g/cm^3, while the density of MDA is ($\rho_{MDA} = 1.06$ g/cm^3).[4] In the case of PIMD simulations, the structure and density of MDA are remarkably similar to the structure and density of the IA produced at $P = 100$ MPa ($\rho_{IA} = 1.06$ g/cm^3 at $T = 80$ K). As shown in Fig. S2 of the supplementary material, the structure of the IA obtained from PIMD simulations at $P = 100$ MPa is very similar to the structure of MDA. We note that the cooling pressure at which the IA matches the structure and density of MDA in classical MD and PIMD simulations ($P = 125$ MPa and $P = 100$ MPa, respectively) differ by $\Delta P = 25$ MPa. This value of ΔP is close to the difference in the corresponding LLCP pressure P_c of classical and quantum q-TIP4P/F water,[98] $\Delta P_c \approx 15$ MPa.

2. Structure of LDA, IA, and HDA

To further understand the role of NQE on the amorphous ices generated by isobaric cooling under pressure, we also calculated the radial distribution function and the local order of the amorphous ices generated at $P = 0.1, 400$, and 1000 MPa. At these pressures, water vitrifies into LDA, IA, and HDA forms, respectively.

The oxygen–oxygen (OO), oxygen–hydrogen (OH), and hydrogen–hydrogen (HH) radial distribution functions (RDFs) of q-TIP4P/F water (H_2O) at $P = 0.1, 400$, and 1000 MPa and

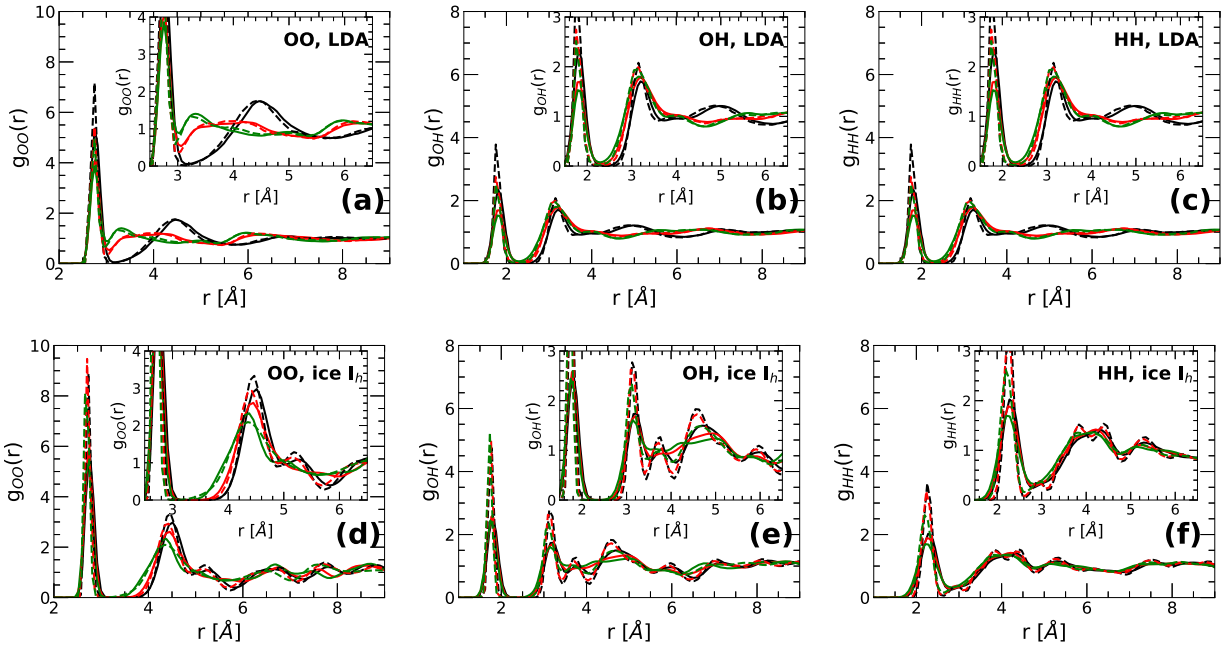

FIG. 2. (a) Oxygen–oxygen (OO), (b) oxygen–hydrogen (OH), and (c) hydrogen–hydrogen RDF of amorphous ice at $P = 0.1$ MPa (black line, LDA), $P = 400$ MPa (red line, IA), and $P = 1000$ MPa (green line, HDA). Dashed and solid lines are obtained from classical MD and PIMD simulations, respectively; $T = 80$ K. (d) OO, (e) OH, and (f) HH RDF of ice I_h at $T = 80$ K obtained from PIMD and classical MD simulations. Line colors and styles are the same used in (a)–(c). Insets are magnifications of the main panels. The inclusion of NQE reduces the height of the OO/OH/HH RDF extrema, leading to a less structured amorphous ice and ice I_h.

$T = 80$ K are shown in Figs. 2(a)–2(c). Included are the RDFs obtained from classical MD (dashed lines) and PIMD (solid lines) simulations. The RDFs obtained from classical and quantum q-TIP4P/F are qualitatively similar to each other, with the RDF maxima located at the same positions. The main difference between MD/PIMD simulations is that including NQE leads to smoother maxima and minima in the RDFs, which is a known effect due to the atom delocalizations.[80,85,86] This is an indication that including NQE leads to less structured environments in amorphous ices. For comparison, we include in Figs. 2(d) and 2(e) the OO, OH, and HH RDFs of ice I_h for the same pressures and temperature of the amorphous ices shown in Figs. 2(a)–2(c). The observed NQE on LDA, IA, and HDA [Figs. 2(a)–2(c)] are not limited to the glass state but are also found in ice I_h [Figs. 2(d) and 2(e)].

Figure 2(a) is particularly important since it clearly depicts the effect of increasing the pressure on the structure of the amorphous ices generated by isobaric cooling, including/excluding NQE. Briefly, both MD and PIMD simulations show that, as the pressure increases, the second maximum located at $r = 4.5$ Å decreases while the first minimum of the OO RDF located at $r \approx 3.2$ Å increases. This implies that the main effect of increasing the cooling pressure is to displace the neighboring water molecules of a central water molecule from its second hydration shell to the first interstitial space (see also Sec. III of the supplementary material for the discussion of the local order of the amorphous ices and ice I_h obtained at $P = 0.1, 400,$ and 1000 MPa).

Overall, the structural changes seen for IA at $T = 80$ K are consistent with previous computational studies of glassy water.[76] Importantly, the OO-RDF of the IA obtained at $P = 100$ MPa is remarkably similar to the corresponding RDF of MDA reported in Ref. 4 (see Fig. S2 of the supplementary material). As shown in Ref. 76, the OO RDF of IA evolves continuously from the OO RDF of LDA to that of HDA as the pressure (and density) increase from $P \approx 0.1$ MPa to $P \approx 1000$ MPa. These conclusions are not affected by the inclusion of NQE.

3. Hydrogen-bonds in LDA, IA, and HDA

The observed NQEs on the RDFs of the amorphous ices obtained by isobaric cooling under pressure suggest that NQE may also affect the geometry of the hydrogen-bonds (HBs) in glassy water. Next, we characterized the hydrogen-bonds (HBs) between water molecules in the LDA, IA, and HDA shown in Figs. 2(a)–2(c); for comparison, we also studied the HB geometry of ice I_h [Figs. 2(d)–2(f)]. To do so, we consider pairs of hydrogen-bonded molecules and focus on the corresponding OO distance $d_{OO}^{HB}(T)$ and HOO angle $\theta_{HOO}^{HB}(T)$. Briefly, two water molecules form a HB if the corresponding OO distance is $d_{OO}^{HB} < 3.5$ Å and the HOO angle is $\theta_{HOO}^{HB} < 30^\circ$ (see Refs. 80 and 102).

Figures 3(a) and 3(b) show $d_{OO}^{HB}(T)$ and $\theta_{HOO}^{HB}(T)$ averaged over all pairs of hydrogen-bonded molecules in the system, $\langle d_{OO}^{HB}(T)\rangle$ and $\langle \theta_{HOO}^{HB}(T)\rangle$, for the LDA, IA, and HDA obtained at $P = 0.1$, 400, and 1000 MPa and $T = 80$ K. At all pressures, PIMD and classical MD provide the same qualitative picture, with $\langle d_{OO}^{HB}(T)\rangle$ and $\langle \theta_{HOO}^{HB}(T)\rangle$ decreasing upon isobaric cooling. This means that the HBs become shorter (smaller $\langle d_{OO}^{HB}(T)\rangle$) and more linear

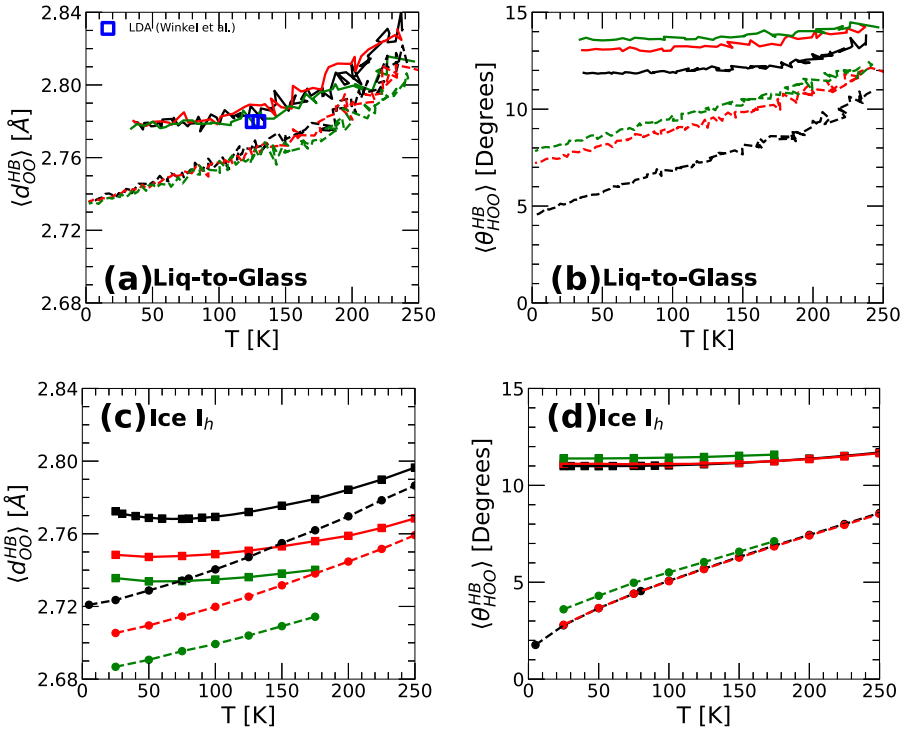

FIG. 3. Average OO distance, $\langle d_{OO}^{HB}(T) \rangle$, and HOO angle, $\langle \theta_{HOO}^{HB}(T) \rangle$, between pairs of hydrogen-bonded water molecules. (a) and (b) Results for water during the vitrification (isobaric cooling) into LDA (P = 0.1 MPa, black line), IA (P = 400 MPa, red line), and HDA (P = 1000 MPa, green line). Solid and dashed lines are results from PIMD and classical MD simulations, respectively. (c) and (d) Same lines as (a) and (b) for ice I_h. In all cases, including NQE (PIMD simulations) leads to longer (larger $\langle d_{OO}^{HB}(T) \rangle$) and less linear (larger $\langle \theta_{HOO}^{HB}(T) \rangle$) HB than found in the classical case (MD simulations). Blue squares in (a) are experimental data from Ref. 103.

(smaller $\langle \theta_{HOO}^{HB}(T) \rangle$) upon cooling, as expected. Interestingly, MD/PIMD simulations both show that the HB length is pressure independent [Fig. 3(a)], while the HOO angle is not [Fig. 3(b)]. In other words, as the cooling pressure increases along the sequence LDA → IA → HDA, one finds that the HB have similar lengths but become increasingly less linear.

At the quantitative level, NQEs on the geometry of the HB are important. Briefly, the delocalization of the O and, particularly, H atoms leads to HB that are (i) longer and (ii) less linear than observed in the classical case. (i) PIMD simulations predict HB that are longer by ≈0.03 Å than observed in classical MD simulations [Fig. 3(a)]. As shown in Fig. 3(a), the experimental HB OO distance in LDA at $T \approx 125$ K [blue squares][103] is in excellent agreement with the PIMD simulations, stressing the relevance of including NQE. Similarly, (ii) NQEs affect the HOO angle considerably. For example, at T = 80 K, including NQE leads to HOO angles that are ~4°–6° larger, depending on the pressure, than predicted by classical MD simulations [Fig. 3(b)]. Hence, the inclusion of NQE leads to less linear HB, which indicates that the HB network is softer than predicted in classical MD simulations (see also Sec. III B 3).

For comparison, we show in Figs. 3(c) and 3(d) the $\langle d_{OO}^{HB}(T) \rangle$ and $\langle \theta_{HOO}^{HB}(T) \rangle$ of ice I_h at P = 0.1, 400, and 1000 MPa. As for the case of the amorphous ices, classical MD and PIMD simulations show that the HBs become shorter and more linear upon cooling. Again, including NQE leads to a weaker HB network characterized by longer and less linear HB than found in classical MD. For example, at T = 80 K, the values obtained for $\langle d_{OO}^{HB}(T) \rangle$ from PIMD simulations are ≈0.03 – 0.04 Å longer than the corresponding values obtained in MD simulations. At the same temperature, the values of $\langle \theta_{OO}^{HB}(T) \rangle$ obtained from PIMD simulations are ≈5 – 6° larger than the corresponding values obtained in classical MD simulations. Increasing the pressure at a given temperature affects mainly the length of the HB in ice I_h; $\langle d_{OO}^{HB}(T) \rangle$ decreases with increasing pressure. Our results are consistent with MD/PIMD computer simulations of density functional theory (DFT)-based machine-learned potentials of liquid water and ice I_h in Ref. 104, where NQE were found to broaden the HB length distribution. Additionally, our results also align with Refs. 105 and 106, which indicates that increasing the O–O distances between water molecules leads to weaker HB when NQE are included.

One may wonder how the HBs in glassy water compare with the HB of ice I_h. A close comparison of Figs. 3(a) and 3(b) with Figs. 3(c) and 3(d) indicates that (i) the HBs of LDA/IA/HDA are slightly longer ($\delta \langle d_{OO}^{HB}(T) \rangle \approx 0.01 - 0.06$ Å at T = 80 K) and (ii) less linear ($\delta \langle \theta_{HOO}^{HB}(T) \rangle \approx 1 - 4°$ at T = 80 K) than found in ice I_h. These observations hold independently of whether NQE are included/excluded (MD and PIMD simulations) and are consistent with the view that the HB network in glassy water is more distorted than in ice.

4. Atoms delocalization in LDA, IA, HDA

In order to quantify the delocalization of the O and H of water in both glassy water and ice I_h, we calculated the average radius of gyration of the corresponding ring-polymers, R_g, from our PIMD simulations. R_g quantifies how extended the ring-polymers are and is given by

$$R_g = \left\langle \frac{1}{n_b} \sum_{k=1}^{n_b} (r_c - r_k)^2 \right\rangle. \quad (1)$$

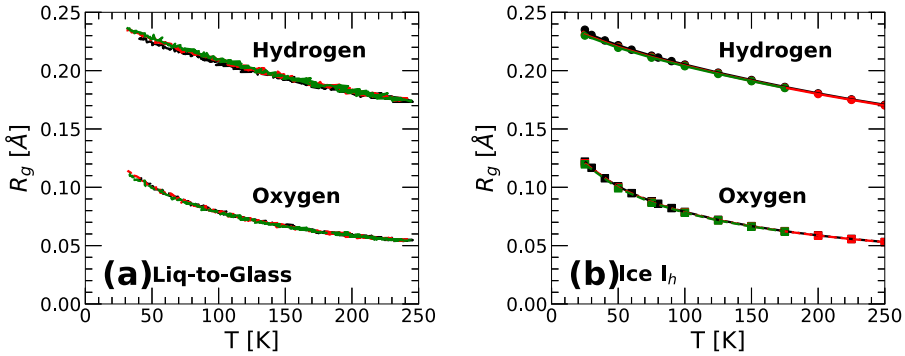

FIG. 4. Radius of gyration $R_g(T)$ of the ring-polymers associated to the O and H atoms obtained from PIMD simulations of q-TIP4P/F water. (a) $R_g(T)$ during the isobaric cooling of liquid water into the glass state at $P = 0.1$ MPa (black lines, LDA), 400 MPa (red lines, IA), and $P = 1000$ MPa (green lines, HDA). (b) Same as (a) for the case of ice, I_h. At all pressures studied, the delocalization of the O and H atoms increases monotonically upon cooling, and it is larger for the H atoms (as expected). The O/H delocalization is independent of the water structure (LDA, IA, HDA, ice I_h) and pressure and depends solely on the temperature of the system.

Here, r_c is the center of mass of a given ring-polymer and r_k is the position of the corresponding bead; $\langle \ldots \rangle$ indicates an average over time and over all ring-polymers in the system (of the same kind, i.e., associated to O or H atoms). For a given atom, R_g quantifies the corresponding delocalization due to NQE.

Figure 4(a) shows the values of $R_g(T)$ for the O and H atoms of q-TIP4P/F water during its vitrification (isobaric cooling) into LDA, IA, and HDA at $P = 0.1, 400,$ and 1000 MPa, respectively. In all cases, $R_g(T)$ increases monotonically upon cooling, in agreement with previous simulations.[80,107] Moreover, at a given pressure and temperature, the H atoms are more delocalized than the O atoms (as expected). Interestingly, we find that the values of $R_g(T)$ for LDA, IA, and HDA practically overlap. This implies that the delocalization of the O/H atoms is independent of pressure and, particularly, of the local environment of the specific amorphous ice considered. This is in agreement with previous studies of water-like model liquids that show a very weak dependence of R_g with pressure.[108,109] The delocalization of the O and H atoms in ice I_h is included in Fig. 4(b). A comparison of Figs. 4(a) and 4(b) shows that the delocalization of the O/H atoms is practically identical in ice I_h and LDA/IA/HDA. Briefly, the delocalization of the O/H atoms due to NQE depends solely on the temperature of the system; it is independent of the pressure applied and, particularly, of the local structure of water (LDA, IA, HDA, ice I_h). We stress that the delocalization of the H atoms in LDA/IA/HDA/ice I_h is non-negligible. Specifically, at $T = 80$ K, $R_g \approx 0.22$ Å for H, implying that the ring-polymer beads associated to the H atoms form a cloud of ≈0.44 Å, i.e., approximately half the length of the OH covalent bond of a water molecule (≈1 Å).

B. Pressure-induced amorphization of ice I_h and LDA–HDA transformations

In this section, we discuss the isothermal compression-induced ice I_h-to-HDA and LDA-to-HDA transformations in H_2O and D_2O using the q-TIP4P/F water model; the corresponding decompression-induced HDA-to-LDA transformations are also studied. LDA is prepared by isobaric cooling liquid water from $T = 240$ K to $T = 35$ K at $P = 0.1$ MPa using a cooling rate of $q_T = 10$ K/ns (for both H_2O and D_2O). The LDA configuration obtained at $T = 80$ K is then isothermally compressed using a compression rate $q_P = 100$ MPa/ns from $P = 0.1$–3000 MPa, resulting in HDA. The HDA configurations are then isothermally decompressed (using the same rate $q_P = 100$ MPa/ns) from $P = 2000$ MPa down to negative pressures until the amorphous ice fractures (at approximately $P < -600$ MPa). The computational details for these out-of-equilibrium simulations of glassy water have become standard; see Refs. 70, 73, 75–77, and 110 for additional details.

1. Density

Figure 5(a) shows the density of H_2O and D_2O as a function of pressure, $\rho(P)$, during the pressure-induced LDA–HDA transformations at $T = 80$ K from PIMD simulations (red and green lines). For comparison, also included is the $\rho(P)$ during the LDA–HDA transformation in H_2O obtained from classical MD (blue lines) simulations. In all cases, upon compression, the density of LDA shows a rapid increase in $\rho(P)$ at $P \approx 800$–1200 MPa, indicating the transformation to HDA, consistent with previous classical MD simulations of rigid/flexible water models[66,73,76] and particularly, experiments.[18,19] The transformation of HDA during decompression is irreversible at $P \geq 0$ MPa, as found in experiments[19,41] ($T = 80$ K). As observed in previous computational studies,[66,70,73,76,77,90,91] HDA transforms rather smoothly to an LDA-like state just before it fractures at $P < -600$ MPa.

The $\rho(P)$ of H_2O and D_2O during the compression-induced ice I_h-to-HDA transformation and subsequent decompression of HDA at $T = 80$ K is included in Fig. 5(b). The transformation of ice I_h to HDA is sharp and occurs at $P \approx 1400$–1800 MPa;[66,73,91,111] upon decompression, the so obtained HDA also transforms rather smoothly to an LDA-like state just before it fractures at $P < -600$ MPa.

A few important points follow from Figs. 5(a) and 5(b). (i) Including NQE in H_2O (PIMD simulations; red line) does not change qualitatively the results from classical MD simulations (blue lines), both showing clear transformations among ice I_h, LDA, and HDA upon isothermal compression/decompression. (ii) PIMD simulations also reproduce the transformations among ice I_h, LDA,

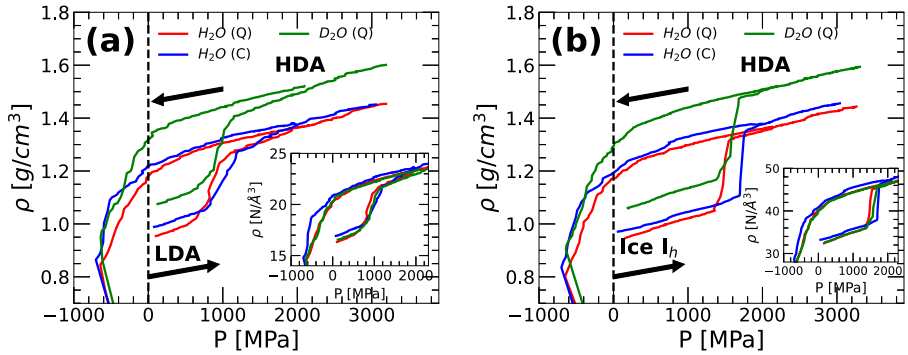

FIG. 5. (a) Density as a function of pressure $\rho(P)$ during the compression-induced LDA-to-HDA transformation at T = 80 K and subsequent decompression of HDA. Results are for H_2O (PIMD simulations, red lines; classical MD simulations, blue lines) and D_2O (PIMD simulations, green lines). The LDA configurations are obtained by isobaric cooling the equilibrium liquid from T = 240 to 80 K at P = 0.1 MPa using a cooling rate of q_T = 10 K/ns. The compression/decompression rate is q_P = 100 MPa/ns. The sudden density increase during compression at $P \approx$ 800–1000 MPa signals the transformation of LDA to HDA. During decompression, HDA transforms smoothly to an LDA-like state before it fractures at $P < -600$ MPa. (b) $\rho(P)$ during the compression-induced ice I_h-to-HDA transformation at T = 80 K and subsequent decompression of HDA (q_P = 100 MPa/ns). Results are for H_2O (PIMD simulations, red lines; classical MD simulations, blue lines) and D_2O (PIMD simulations, green lines). The sudden density increase during compression at $P \approx$ 1400–1800 MPa signals the transformation of ice I_h to HDA; during decompression, HDA transforms smoothly to an LDA-like state before it fractures.

and HDA in D_2O, consistent with experiments (green lines).[35,112] (iii) To remove the effects of the different molecular masses m of H_2O and D_2O, we also include in the insets of Figs. 5(a) and 5(b) the *number* density $\rho_n(P) \equiv \rho(P)/m$ obtained from the $\rho(P)$ shown in the corresponding main panels. The behavior of $\rho_n(P)$ during the transformations among ice I_h, LDA, and HDA in H_2O and D_2O are remarkably close to one another. This suggests that, at the molecular level, the same structural changes occur in H_2O, with and without NQE included, and in D_2O. This strongly indicates that the LDA-to-HDA and ice I_h-to-HDA are accompanied by a similar collapse of the hydrogen-bond (HB) network in H_2O and D_2O (see discussion below). (iv) The inset of Fig. 5(b) shows that the specific I_h-to-HDA transition in H_2O, with and without NQE included, occurs at different pressures, $P_{Ih-to-HDA}$. Specifically, $P_{Ih-to-HDA} \approx$ 1400 MPa in PIMD simulations (red lines), while $P_{Ih-to-HDA} \approx$ 1800 in classical MD simulations (blue lines). This decrease in $P_{Ih-to-HDA}$ by ~≈400 MPa when NQE are included strongly indicates that the inclusion of NQE weakens the HB of H_2O, facilitating the collapse of the HB network at lower pressures during the compression process. Similar conclusions seem to follow from the inset of Fig. 5(a) during the LDA-to-HDA transformation H_2O. In this case, the LDA-to-HDA transition pressure of H_2O decreases by ≈100 MPa when NQE are included, although the $\rho_n(P)$ in Fig. 5(a) is noisy. The results obtained during the decompression of HDA in H_2O from PIMD and classical MD simulations are also consistent with NQE weakening the HB in H_2O. The insets of Figs. 5(a) and 5(b) show that including NQE decreases the *magnitude* of the HDA-to-LDA transformation pressure (red and blue lines) by ≈100 – 200 MPa. This means that during decompression, HDA transforms earlier (lower tension) to an LDA-like state.

The behavior of $\rho_n(P)$ for D_2O during the ice-to-HDA and LDA-to-HDA transformations falls in between the corresponding $\rho_n(P)$ obtained for H_2O in PIMD and classical MD simulations. Hence, the HB and associated HB network increase in strength along the sequence "quantum H_2O (PIMD simulations) → D_2O → classical H_2O (MD simulations)."

2. Molecular structure of LDA and HDA

To characterize the structure of LDA and HDA, we focus on two properties, the oxygen–oxygen radial distribution function (OO RDF) and the local order parameter d_{sf} introduced in Ref. 113. The OO RDF of LDA and HDA at P = 0.1 MPa and T = 80 K for both H_2O and D_2O are shown in Fig. 6(a). The LDA and HDA forms are obtained during the compression/decompression cycles shown in Fig. 5(a). The OO RDF obtained in our classical/MD simulations for H_2O are both in good agreement with the experimental RDF reported in Refs. 38 and 114. Including NQE (PIMD simulations) reduces slightly the maxima of the OO RDF of LDA and HDA, improving slightly the RDF relative to the experiments. It follows that including NQE makes H_2O slightly less structured, supporting the view that including NQE weakens the HB network of water (see Sec. III B 1 and Fig. 5). For comparison, we include in Fig. 6(b) the OO RDF of ice I_h and HDA at P = 0.1 MPa and T = 80 K obtained during the ice I_h-HDA compression/decompression cycles shown in Fig. 5(b). A comparison of Figs. 6(a) and 6(b) shows that while the RDF of LDA and ice I_h are clearly different, the OO RDF of HDA produced by compressing LDA and ice I_h are barely indistinguishable from one another.

The order parameter d_{fs} is defined in Ref. 113 and was used previously to characterize the local structure of q-TIP4P/F water from classical MD and PIMD simulations (see Ref. 80). Briefly, for molecule i, $d_{fs,i}$ is the difference between (i) the distance from the given molecule to its fifth nearest neighbor and (ii) the distance from the given molecule to its fourth nearest neighbor. Hence, $d_{fs,i}$ quantifies the distance between the first and second hydration shells of molecule i (see also Sec. III of the supplementary material for the definition of d_{fs}).

Figures 7(a) and 7(b) show the average order parameter $\langle d_{fs} \rangle$ as a function of pressure during the LDA–HDA and ice I_h-HDA

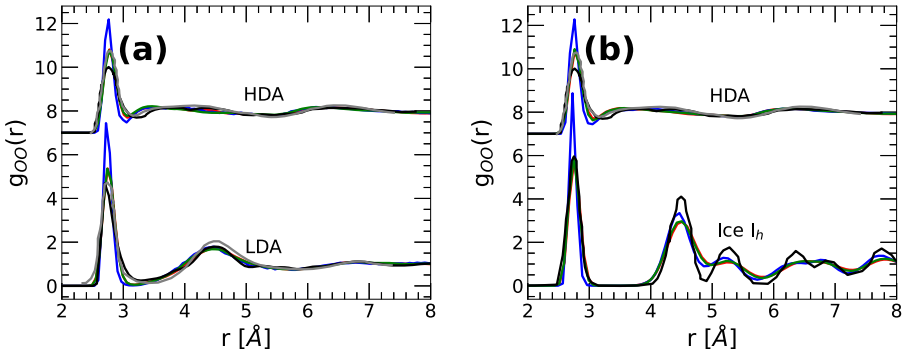

FIG. 6. (a) Comparison of the OO radial distribution function of LDA and HDA at $P = 0.1$ MPa and $T = 80$ K from experiments and from our classical MD and PIMD simulations using the q-TIP4P/F water model. LDA was obtained by isobaric cooling at $P = 0.1$ MPa, and the HDA was obtained by the isothermal compression–decompression cycle shown in Fig. 5(a). (b) Comparison of the OO RDF of ice I_h and HDA obtained from computer simulations with experiments at $P = 0.1$ MPa and $T = 80$ K. The HDA was obtained from the isothermal compression–decompression cycle shown in Fig. 5(b). The black and gray lines in (a) correspond to the experimental OO RDF of LDA and HDA from Refs. 114 and 38, respectively. Similarly, the black and gray lines in (b) correspond to the experimental OO RDF of ice I_h and HDA from Refs. 38, 114, and 115. Red, blue, and green are the RDFs obtained from classical MD and PIMD simulations of H_2O and D_2O (same colors as in Fig. 5).

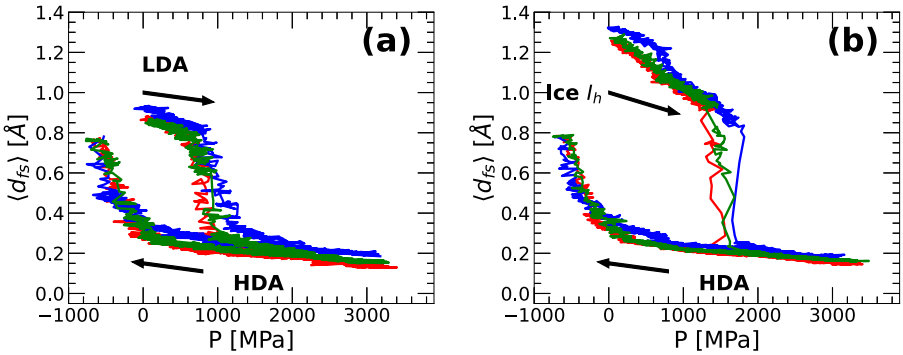

FIG. 7. Average local order parameter $\langle d_{fs} \rangle$ as a function of pressure during the (a) LDA–HDA compression/decompression cycle shown in Fig. 5(a) and (b) ice I_h-HDA compression/decompression cycle shown in Fig. 5(b) ($T = 80$ K and $q_P = 100$ MPa/ns). Results are from classical MD and PIMD simulations of H_2O and D_2O; colors are the same as in Fig. 5.

compression/decompression cycles shown in Figs. 5(a) and 5(b) ($T = 80$ K and $q_P = 100$ MPa/ns). The same qualitative behavior for $\langle d_{fs} \rangle$ follows from classical/quantum H_2O and D_2O. For example, Fig. 7(a) shows that, during compression, $\langle d_{fs} \rangle$ suddenly decreases from ≈0.8 – 0.9 Å (LDA) to ≈0.3 Å (HDA). Similarly, Fig. 7(b) shows that, during compression, $\langle d_{fs} \rangle$ suddenly decreases from ≈1.4 – 0.9 Å (ice I_h) to ≈0.3 Å (HDA). Interestingly, both transformations to HDA occur when $\langle d_{fs} \rangle \approx 0.8 - 0.9$ Å. This suggests that the collapse of the HB network of LDA and ice I_h occurs when the same level of local disorder is achieved during the compression process, independently of the starting state of water (LDA or ice I_h); see also Ref. 73. Figures 7(a) and 7(b) also show that, during the decompression of HDA, $\langle d_{fs} \rangle$ increases smoothly with decreasing pressure.

The similarities in the behavior of $\rho(P)$ in Figs. 5(a) and 5(b) and $\langle d_{fs} \rangle$ in Figs. 7(a) and 7(b) are self-evident. It follows that during the compression of LDA/ice I_h to HDA, the second hydration shell of water collapses and a water molecule moves from the second hydration shell toward the first interstitial shell, in agreement with Figs. 6(a) and 6(b) and previous studies.[66,73,76] The important point from Fig. 7 is that this molecular-level picture underlying the ice I_h-HDA and LDA–HDA transformations holds independently of whether NQE are included and applies to both H_2O and D_2O. Consistent with Fig. 5, the sudden decrease of $\langle d_{fs} \rangle$ during the ice I_h-to-HDA and LDA-to-HDA transformations occurs at slightly different pressures when NQE are included/excluded. The corresponding ice I_h/LDA-to-HDA transition pressures increase along the sequence "quantum $H_2O \rightarrow D_2O \rightarrow$ classical H_2O," again suggesting that the HB network of water becomes softer as NQE are included.

3. Hydrogen-bonding in LDA and HDA

Figures 8(a) and 8(b) show $\langle d_{OO}^{HB} \rangle$ and $\langle \theta_{HOO}^{HB} \rangle$ during the compression/decompression LDA–HDA cycles included in Figs. 5(a) and 5(b). In all cases, classical/quantum H_2O and D_2O, $\langle d_{OO}^{HB} \rangle$ decreases monotonically up to $P \approx 800$ MPa, where LDA transforms to HDA. In addition, $\langle \theta_{HOO}^{HB} \rangle$ remains practically constant. Hence, during the compression of LDA, the HB becomes shorter, but the linearity of the HB remains unaffected. The average HB length in LDA decreases by ≈0.03 Å ($P = 0.1$–800 MPa), which is not negligible. The LDA-to-HDA transformation is accompanied by an increase in $\langle d_{OO}^{HB} \rangle$ of ≈0.02 – 0.04 Å and an increase in $\langle \theta_{HOO}^{HB} \rangle$ of ≈2 – 3°. In other words, during the LDA-to-HDA transformation, the HB in classical/quantum H_2O and D_2O becomes longer

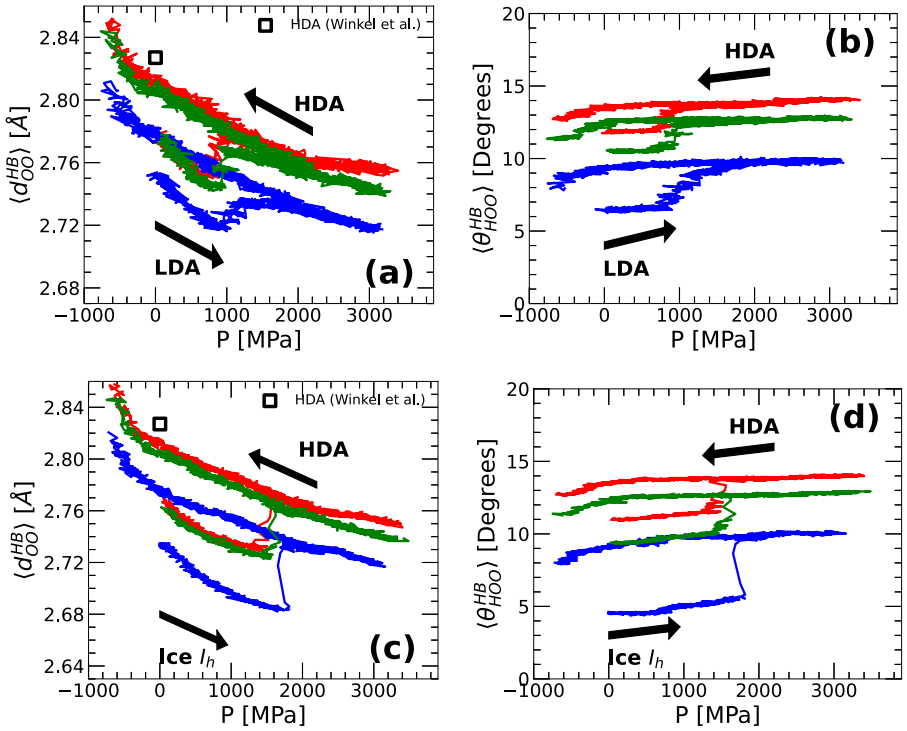

FIG. 8. Average OO distance $\langle d_{OO}^{HB} \rangle$ and HOO angle $\langle \theta_{HOO}^{HB} \rangle$ between pairs of water molecules forming a HB. (a) $\langle d_{OO}^{HB} \rangle$ and $\langle \theta_{HOO}^{HB} \rangle$ as a function of pressure during the compression/decompression-induced LDA–HDA transformations at $T = 80$ K ($q_P = 100$ MPa/ns); see Fig. 5(a). (c) and (d) Same as (a) and (b) during the ice compression/decompression-induced I_h-HDA transformations; see Fig. 5(b). Results are from classical and quantum H_2O as well as D_2O; color lines are the same as in Fig. 5. Counterintuitively, during the LDA-to-HDA and ice I_h-to-HDA transitions, $\langle d_{OO}^{HB} \rangle$ increases, even when the system becomes denser (see text). The inclusion of NQE leads to longer (larger $\langle d_{OO}^{HB} \rangle$) and less linear HB (larger $\langle \theta_{HOO}^{HB} \rangle$) in ice I_h, LDA, and HDA than predicted by classical MD simulations at all pressures studied. The black squares in (a) and (c) correspond to the experimental data for the HB OO distance for HDA from Ref. 103.

and less linear. Similar changes in the HB geometry are found during the compression-induced ice I_h-to-HDA transition; see Figs. 8(c) and 8(d).

The observed changes in the HB geometry are counterintuitive since, during both the LDA-to-HDA and ice I_h-to-HDA transformations, the density increases considerably (by ≈25 – 35%) (see Fig. 5), but the molecules get further apart on average (Figs. 6 and 7). The following counterintuitive picture is as follows. During the compression of LDA and ice I_h, the fifth nearest neighbor of a given water molecule moves from the corresponding second hydration shell ($r_2 \approx 4.5$ Å, Fig. 6) toward its first hydration shell ($r_1 \approx 2.8$ Å, Fig. 6), populating the associated first interstitial shell ($r^* \approx 3.2$ Å, Fig. 6). This fifth nearest neighbor (of the given molecule) does not form a HB with the given water molecule (a given water molecule only forms ≈4 HB with its four nearest water molecules located in the first hydration shell). Therefore, as the fifth nearest neighbor gets closer to the given molecule, the corresponding ≈4 hydrogen-bonded nearest neighbors move further away (in average), and the HB becomes less linear (distorted), giving room to the incoming water molecule. As a result, the whole process leads to more compact local environments.

During the decompression of HDA, $\langle d_{OO}^{HB} \rangle$ increases monotonically with decreasing pressure [Figs. 8(a) and 8(b)], i.e., the HB becomes longer, while $\langle \theta_{HOO}^{HB} \rangle$ remains constant or decreases slightly (by ≈1° at very negative pressures) [Figs. 8(c) and 8(d)].

While the overall picture described earlier holds for classical and quantum H_2O, as well as D_2O, the inclusion of NQE plays a relevant role on the properties of the HB. Specifically, including NQE in H_2O increases $\langle d_{OO}^{HB} \rangle$ by ≈0.03 – 0.04 Å at all pressures studied during the LDA–HDA compression/decompression cycle [the red lines in Fig. 8(a) practically overlap with the blue lines if shifted by ≈ – 0.03 Å along the y axis]. Similarly, including NQE increases $\langle \theta_{HOO}^{HB} \rangle$ by ≈4 – 6° at all pressures studied during the LDA–HDA compression/decompression cycle [see the red and blue lines in Fig. 8(b)]. The same conclusions apply to the HB of H_2O during the ice I_h-HDA compression/decompression cycle [Figs. 8(c) and 8(d)]. Briefly, relative to the classical case, including NQE leads to longer and less linear HB in ice I_h, LDA, and HDA at $T = 80$ K and for all pressures studied. These NQEs on the geometry of the HB in ice/glassy water are consistent with the view where the HB network of water becomes softer. We note that the experimental values of $\langle d_{OO}^{HB} \rangle$ for LDA and HDA at $P = 0.1$ MPa are closer to the results obtained from PIMD simulations than MD simulations; see Figs. 3(a), 8(a), and 8(c), respectively. This stresses the relevance of NQE for a *quantitative* description of ice and glassy water.

4. Atoms delocalization in LDA and HDA

The results discussed earlier show that, in the case of LDA, HDA, and ice I_h, the structural and thermodynamic properties obtained from classical MD (no NQE) and PIMD (NQE included) are different. Not surprisingly, the different results obtained from PIMD and classical MD simulations are due to the delocalization of the H/D atoms. Here, we quantify the atom delocalization in water during the pressure-induced LDA–HDA and ice I_h–HDA transformations studied. We calculate the pressure-dependence of the radius of gyration $R_g(P)$ of the ring-polymers associated to the O and H/D atoms of H_2O and D_2O.

Figure 9(a) shows the $R_g(P)$ of O and H/D during the pressure-induced LDA–HDA transformations shown in Fig. 5(a).

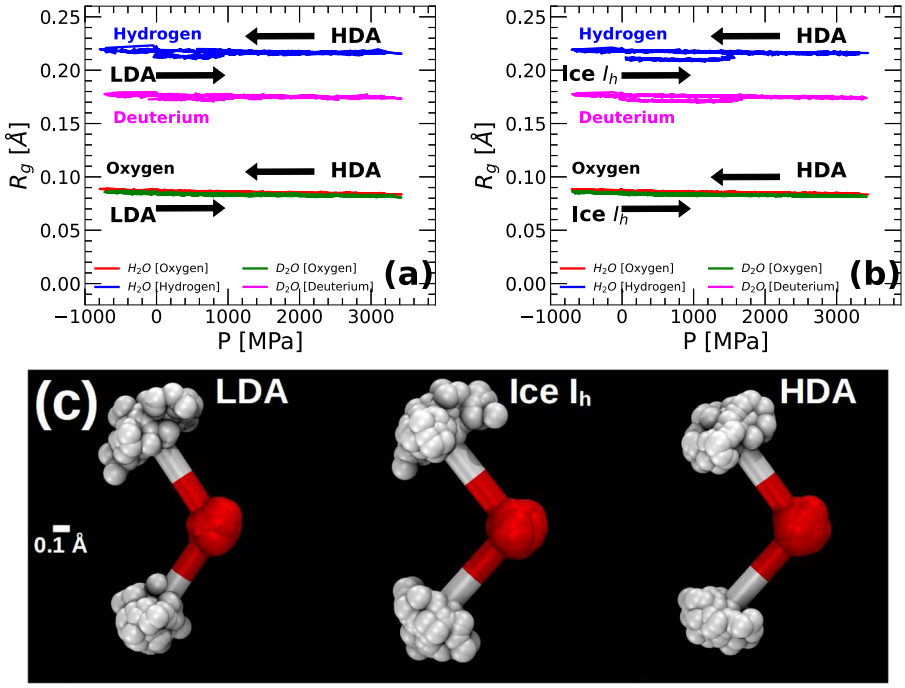

FIG. 9. Radius of gyration $R_g(P)$ of the ring-polymers associated to the O and H/D atoms as a function of pressure during the pressure-induced (a) LDA–HDA and (b) ice I_h-HDA transformation at $T = 80$ K and $q_P = 100$ MPa/ns. Blue and red lines are the values of $R_g(P)$ for the O and H atoms of H_2O. Magenta and green lines correspond to the values of $R_g(P)$ for the O and D atoms of D_2O. The delocalization of the O and H atoms in H_2O is identical during the LDA–HDA and ice I_h-HDA transformations; similarly, the delocalization of the O and D atoms of D_2O is identical during the LDA–HDA and ice I_h-HDA transformations. During the compression of LDA (and ice I_h), the H and D atoms show a small but noticeable sudden increase during the transformation to HDA, similar to results obtained from PIMD simulations using a water-like model.[107] (c) Snapshot of an H_2O molecule in LDA, ice I_h, and HDA obtained from PIMD simulations at $P = 0.1$ MPa and $T = 80$ K. The ring-polymer beads associated to the O and H atoms are represented by white and red spheres, respectively (ring-polymers are composed of $n_b = 128$ beads); the same length scale is used in all snapshots (bar corresponds to 0.1 Å). The delocalization of the H atoms is preferentially along the directions perpendicular to the corresponding OH covalent bond.

Our PIMD simulations indicate that the O atoms of H_2O and D_2O are barely delocalized, $R_g(P) \approx 0.08$–0.09 Å, and are barely affected by pressure. It follows that the ring-polymers associated with the O atoms spread over a distance of $\approx 0.16 - 0.18$ Å ($\approx 15 - 20\%$ of the O–H covalent bond length). Not surprisingly, the delocalization of the H/D atoms is larger than observed in the case of the O atoms. Figure 9(a) shows that $R_g(P) \approx 0.21$–0.22 Å and $R_g(P) \approx 0.17$–0.18 Å for the H and D atoms, respectively, corresponding to ring-polymers of diameter $\approx 0.42 - 0.44$ Å and $\approx 0.34 - 0.36$ Å. This implies that the delocalization of the H and D atoms in ice I_h/LDA/HDA corresponds, respectively, to ≈35% and 45% of the OH covalent bond length ($T = 80$ K).

Interestingly, the delocalization of the O atoms during the LDA–HDA cycle is reversible, while the delocalization of the H/D atoms is not. Figure 9(a) shows that the $R_g(P)$ associated with the O atoms overlaps during the compression and decompression processes. Instead, the $R_g(P)$ associated to the H/D atoms increases suddenly during the LDA-to-HDA transformation, at $P \approx 800$ MPa, and remains practically constant during the decompression of HDA. Strictly speaking, this implies that the delocalization of the H/D atoms is greater in HDA than in LDA, while the delocalization of the O atoms is the same as in LDA and HDA. Yet, the changes in the delocalization of H/D in LDA and HDA are very small. From a conceptual point of view, our results indicate that the glass polyamorphism in water imprints a signature in glassy water at the quantum mechanical level, i.e., in the delocalization of the H/D atoms as the system evolves between LDA and HDA. A similar but more pronounced effect was observed in the atom delocalization of a water-like monoatomic system that also exhibits an LDA–HDA transformation.[107]

For comparison, included in Fig. 9(b) are the $R_g(P)$ of the O and H/D atoms during the pressure-induced ice I_h-HDA transformation shown in Fig. 5(b). The same conclusions based on the LDA–HDA transition cycle [Fig. 9(a)] apply to the ice I_h-HDA transformation [Fig. 9(b)]. Figure 9(c) shows a snapshot of a single H_2O molecule in the LDA, ice I_h, and HDA states obtained from the compression of LDA at $P = 0.1$ MPa and $T = 80$ K. Consistent with Figs. 9(a) and 9(b), the delocalization of the O and H atoms is practically the same for all different states. We note that the delocalization of the H atoms in either the LDA/ice I_h/HDA state is preferentially perpendicular to the OH covalent bond, consistent with Ref. 80. In Fig. 10, we include a snapshot of H_2O in the LDA, HDA, and ice I_h states at $P = 0.1$ MPa and $T = 80$ K.

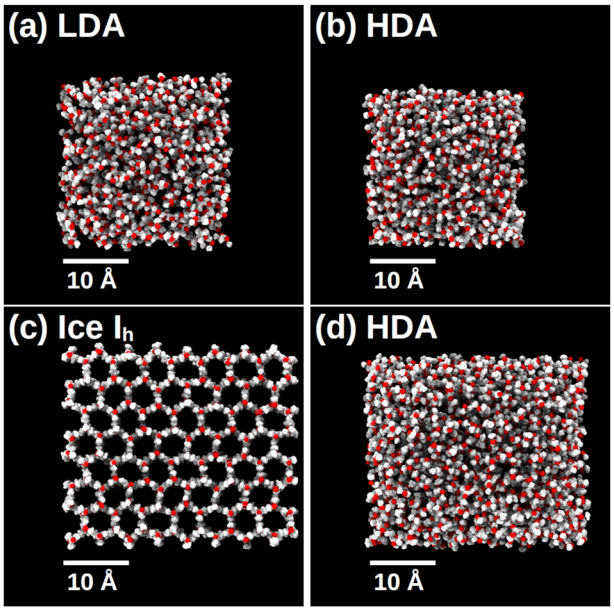

FIG. 10. Snapshot of LDA, HDA, and ice I_h at $P = 0.1$ MPa and $T = 80$ K obtained from PIMD simulations. (a) LDA and (b) HDA formed during the LDA–HDA compression/decompression cycle shown in Fig. 5(a). (c) Ice I_h and (d) HDA formed during the ice I_h-HDA compression/decompression cycle shown in Fig. 5(b). The system in (a) and (b) is composed of $N = 512$ water molecules; $N = 1024$ in (c) and (d). The ring-polymer beads associated with the O and H atoms are shown by red and white spheres, respectively. In all cases, the ring-polymers are composed of $n_b = 128$ and the snapshots are based on the same length scale (bars correspond to 10 Å).

IV. SUMMARY AND DISCUSSION

In this work, we performed classical MD and PIMD simulations of H_2O and D_2O to study the NQE on amorphous ice under pressure. We focused on (A) the vitrification of water during isobaric cooling at different pressures and (B) the ice I_h-HDA and LDA–HDA transformations induced by compression/decompression at cryogenic temperatures.

Our MD/PIMD simulations show that the vitrification (isobaric cooling) of H_2O and D_2O leads to a continuum of amorphous ices [intermediate amorphous ices (IA)] (see Fig. 1). By tuning the cooling pressure, one can generate IA with densities in between those of LDA and HDA. Our results for H_2O, including NQE, are qualitatively similar to those reported in our previous study[76] based on classical MD simulations of q-TIP4P/F water. As discussed there, by carefully choosing the cooling pressure, it is possible to generate IAs that are structurally identical to the recently discovered medium-density amorphous ice (MDA).[4]

It is also found that for all pressures considered in this work, the densities of the amorphous ices (LDA, IA, and HDA) are very sensitive to the inclusion/exclusion of NQE. Results from classical MD and PIMD simulations lead to very different $\rho(T)$ for glassy water as well as ice I_h (Fig. 1); see also Refs. 80, 82, and 116. Interestingly, the structure of the amorphous ices (LDA, IA, and HDA) at $T = 80$ K is weakly affected by the inclusion of NQE (Fig. 2). Yet, including NQE leads to longer (≈0.05 Å) and less linear HB (≈6°) in LDA, IA, and HDA (as well as in ice I_h) (Fig. 3). The differences in the properties of amorphous ice and ice I_h clearly originate in the delocalization of the O and H/D atoms, particularly the later. Interestingly, at a given temperature, the delocalization of the O and H/D atoms in the amorphous ices generated by isobaric cooling is practically independent of the cooling pressure and hence of the local environment of the water molecules (LDA-, IA-, of HDA-like) (Fig. 4).

Our results indicate that the inclusion of NQE does not change qualitatively the out-of-equilibrium phase diagram of amorphous ice that has been reported in previous classical MD simulations.[66,67,73] However, including NQE leads to a better quantitative agreement with available experimental data. To highlight the quantitative impact of NQE in glassy water, we summarize our results in the "phase diagrams" for glassy water (included in Fig. 11; similar phase diagrams have been reported from classical MD simulations of ST2, TIP4P/2005, and TIP4P/Ice[66,67,73,91]). Included are the pressure-induced transformations studied in this work, specifically, (i) the pressures at which LDA transform to HDA during isothermal compression [right green triangles; from Fig. 5(a) and Figs. S4(a) and S4(c) in the supplementary material]; (ii) the pressures at which ice I_h transform to HDA during isothermal compression [right magenta triangles; from Fig. 5(b) and Figs. S4(b) and S4(d) in the supplementary material]; (iii) the pressures at which HDA transforms to an LDA-like state during isothermal decompression [left blue triangles; from Fig. 5(a) and Figs. S4(a) and S4(c) in the supplementary material]; and (iv) the pressures at which such an LDA-like form fractures during further isothermal decompression [left maroon triangles; from Fig. 5(a) and Figs. S4(a) and S4(c) in the supplementary material]. For comparison, also included are (i′) the LLCP and LLPT line for q-TIP4P/F water estimated using the two-state-equation-of-state (TSEOS) in Refs. 44, 46, 50, 60, 61, 64, and 98 (red star and solid black line), as well as the (ii′) liquid-to-vapor spinodal (black squares).[117] As shown in previous MD simulations,[66,67,72,73] the LDA-to-HDA (right green triangles) and HDA-to-LDA (left blue triangles) approach the LLCP with increasing temperature. For comparison, also included in Fig. 11 are the estimated limits of the stability of ice I_h (orange and brown squares). Specifically, we perform numerous 2 ns-long MD/PIMD simulations of ice I_h at different temperatures and pressures and identify those states at which ice I_h melts (orange squares) or sublimates/fractures (brown squares).

Interestingly, the estimated limit of stability of ice I_h to the liquid state (orange squares) merges with the (compression-induced) ice I_h-to-HDA transformation pressure line (magenta right triangles) at the studied compression rates.[73] Experiments show that the melting line of ice I_h (orange line) and the ice I_h-to-HDA transformation line (magenta line) are shifted in pressure relative to one another and connect smoothly at the glass transition temperature of HDA.[118] Within the noise of our data, it remains unclear whether our MD/PIMD simulations reproduce this finding (see also Ref. 73). Interestingly, our data suggest that the melting line of ice I_h (orange line) intersects the sublimation line (brown line) of ice I_h at the intersection of the liquid-to-vapor spinodal line (black line). For comparison, we include in Fig. 11(c) both phase diagrams from Figs. 11(a) and 11(b). Including NQE leads to a small shift in the pressure-induced transformation lines

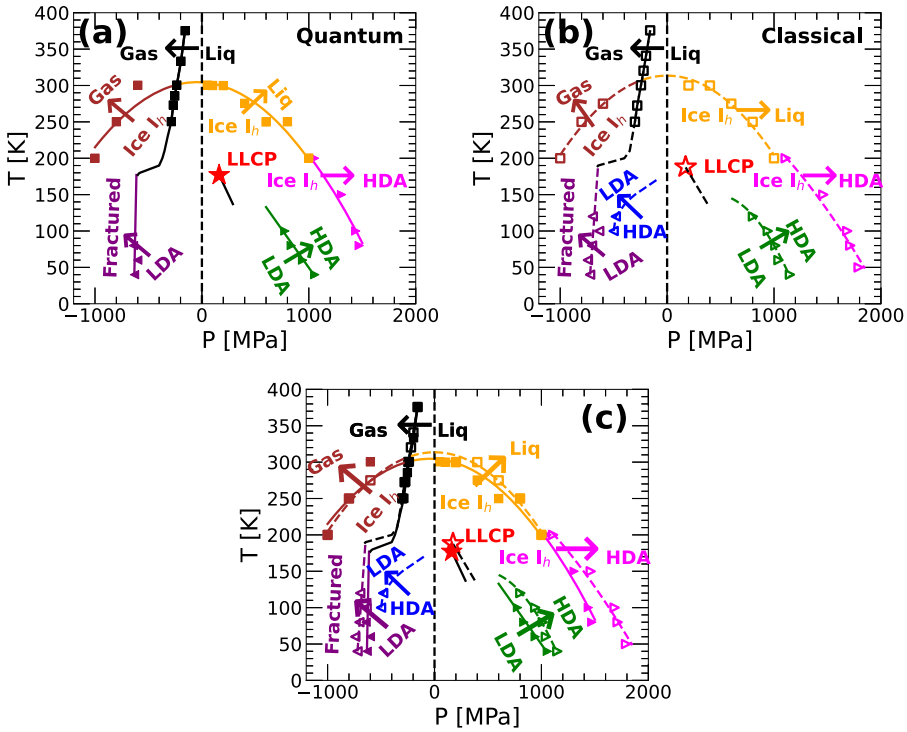

FIG. 11. Phase diagram of glassy water obtained from (a) PIMD and (b) classical MD simulations using the q-TIP4P/F model. The compression (right-triangles) and decompression (left-triangles) transformation pressures are obtained using a rate of q_P = 100 MPa/ns. The green and magenta triangles represent the compression-induced LDA-to-HDA and ice I_h-to-HDA transformations, respectively. The blue and maroon triangles correspond, respectively, to the decompression-induced HDA-to-LDA and fracture of LDA upon further decompression [the HDA-to-LDA transformation pressure (blue triangles) can be detected clearly only in the case of classical MD, and hence they are not included in (a)]. The black squares represent the liquid-to-vapor spinodal of q-TIP4P/F water reported in Ref. 117. The orange and brown squares are estimates for the limit of stability of ice I_h relative to the liquid and gas states, respectively (see text). The red star is the LLCP obtained from the two-state-equation-of-state. (c) Phase diagram of glassy water obtained from (a) PIMD and (b) classical MD simulations. NQEs due to atom delocalization shift the magnitude of the pressured-induced transformation lines of q-TIP4P/F glassy water to lower values.

(by ≈100 – 300 MPa) as well as a small shift in the location of the LLPT and LLCP.

SUPPLEMENTARY MATERIAL

In the supplementary material, we include additional results from PIMD and classical MD simulations using the q-TIP4P/F model, where we show the (i) density maxima of ice I_h at different pressures, (ii) compare the OO RDF of IA obtained using a cooling pressure of 100 MPa with MDA, (iii) discuss the local order metric ($\langle d_{fs} \rangle$) of ice I_h and amorphous ices obtained from isobaric cooling, and (iv) show the LDA-to-HDA and ice I_h-to-HDA compression/decompression cycles obtained at different temperatures.

ACKNOWLEDGMENTS

This work was supported by the SCORE Program of the National Institutes of Health under Award No. 1SC3GM139673 and the NSF CREST Center for Interface Design and Engineered Assembly of Low Dimensional Systems (IDEALS), NSF Grant Nos. HRD-1547380 and HRD-2112550. A.E. is supported by the NSF CREST Postdoctoral Research Program under Award No. 2329339. N.G. acknowledges the support from the NSF Grant No. CHE-2223461. This work used computational resources at San Diego Supercomputer Center (SDSC) through allocation Grant No. CHE230026 from the Advanced Cyberinfrastructure Coordination Ecosystem: Services & Support (ACCESS) program, which is supported by National Science Foundation Grant Nos. 2138259, 2138286, 2138307, 2137603, and 2138296.[119]

AUTHOR DECLARATIONS

Conflict of Interest

The authors have no conflicts to disclose.

Author Contributions

Ali Eltareb: Conceptualization (equal); Data curation (equal); Formal analysis (equal); Methodology (equal); Writing – original draft (equal); Writing – review & editing (equal). **Bibi A. Khan**: Conceptualization (equal); Data curation (equal); Formal analysis

(equal); Writing – original draft (equal); Writing – review & editing (equal). **Gustavo E. Lopez**: Conceptualization (equal); Funding acquisition (equal); Methodology (equal); Supervision (equal); Writing – original draft (equal); Writing – review & editing (equal). **Nicolas Giovambattista**: Conceptualization (equal); Funding acquisition (equal); Methodology (equal); Supervision (equal); Writing – original draft (equal); Writing – review & editing (equal).

DATA AVAILABILITY

The data that support the findings of this study are available within the article and its supplementary material.

REFERENCES

[1] P. G. Debenedetti, *Metastable Liquids: Concepts and Principles* (Princeton University Press, 1996).
[2] F. Franks, *Water: A Matrix of Life* (Royal Society of Chemistry, 2007).
[3] Y. Levy and J. N. Onuchic, Annu. Rev. Biophys. Biomol. Struct. **35**, 389 (2006).
[4] A. Rosu-Finsen, M. B. Davies, A. Amon, H. Wu, A. Sella, A. Michaelides, and C. G. Salzmann, Science **379**, 474 (2023).
[5] T. M. Gasser, A. V. Thoeny, A. D. Fortes, and T. Loerting, Nat. Commun. **12**, 1128 (2021).
[6] C. G. Salzmann, J. Chem. Phys. **150**, 060901 (2019).
[7] C. G. Salzmann, J. S. Loveday, A. Rosu-Finsen, and C. L. Bull, Nat. Commun. **12**, 3162 (2021).
[8] T. Loerting, K. Winkel, M. Seidl, M. Bauer, C. Mitterdorfer, P. H. Handle, C. G. Salzmann, E. Mayer, J. L. Finney, and D. T. Bowron, Phys. Chem. Chem. Phys. **13**, 8783 (2011).
[9] K. H. Kim, K. Amann-Winkel, N. Giovambattista, A. Späh, F. Perakis, H. Pathak, M. L. Parada, C. Yang, D. Mariedahl, T. Eklund *et al.*, Science **370**, 978 (2020).
[10] K. Amann-Winkel, K. H. Kim, N. Giovambattista, M. Ladd-Parada, A. Späh, F. Perakis, H. Pathak, C. Yang, T. Eklund, T. J. Lane *et al.*, Nat. Commun. **14**, 442 (2023).
[11] O. Mishima and H. E. Stanley, Nature **392**, 164 (1998).
[12] O. Mishima, J. Chem. Phys. **133**, 144503 (2010).
[13] R. Shi and H. Tanaka, Proc. Natl. Acad. Sci. U. S. A. **117**, 26591 (2020).
[14] J. Bachler, J. Giebelmann, and T. Loerting, Proc. Natl. Acad. Sci. U. S. A. **118**, e2108194118 (2021).
[15] O. Mishima and T. Sumita, J. Phys. Chem. B **127**, 1414 (2023).
[16] A. Nilsson and L. G. Pettersson, Nat. Commun. **6**(1), 8998 (2015).
[17] O. Mishima, L. Calvert, and E. Whalley, Nature **310**, 393 (1984).
[18] O. Mishima, L. Calvert, and E. Whalley, Nature **314**, 76 (1985).
[19] O. Mishima, J. Chem. Phys. **100**, 5910 (1994).
[20] K. Amann-Winkel, R. Böhmer, F. Fujara, C. Gainaru, B. Geil, and T. Loerting, Rev. Mod. Phys. **88**, 011002 (2016).
[21] P. H. Handle, T. Loerting, and F. Sciortino, Proc. Natl. Acad. Sci. U. S. A. **114**, 13336 (2017).
[22] C. A. Angell, Annu. Rev. Phys. Chem. **55**, 559 (2004).
[23] T. Loerting, V. Fuentes-Landete, P. H. Handle, M. Seidl, K. Amann-Winkel, C. Gainaru, and R. Böhmer, J. Non-Cryst. Solids **407**, 423 (2015).
[24] E. Mayer, J. Appl. Phys. **58**, 663 (1985).
[25] E. Burton and W. Oliver, Proc. R. Soc. A **153**, 166 (1935).
[26] C. Venkatesh, S. Rice, and A. Narten, Science **186**, 927 (1974).
[27] K. P. Stevenson, G. A. Kimmel, Z. Dohnalek, R. S. Smith, and B. D. Kay, Science **283**, 1505 (1999).
[28] G. A. Kimmel, K. P. Stevenson, Z. Dohnalek, R. S. Smith, and B. D. Kay, J. Chem. Phys. **114**, 5284 (2001).
[29] J. H. Cartwright, B. Escribano, and C. I. Sainz-Diaz, Astrophys. J. **687**, 1406 (2008).
[30] K. Kina, Y. Ono, D. Yoshida, and T. Ikeda-Fukazawa, J. Phys. Chem. C **128**, 7806 (2024).
[31] C. Mitterdorfer, M. Bauer, T. G. Youngs, D. T. Bowron, C. R. Hill, H. J. Fraser, J. L. Finney, and T. Loerting, Phys. Chem. Chem. Phys. **16**, 16013 (2014).
[32] H. Li, A. Karina, M. Ladd-Parada, A. Spah, F. Perakis, C. Benmore, and K. Amann-Winkel, J. Phys. Chem. B **125**, 13320 (2021).
[33] O. Mishima and Y. Suzuki, J. Chem. Phys. **115**, 4199 (2001).
[34] K. Winkel, E. Mayer, and T. Loerting, J. Phys. Chem. B **115**, 14141 (2011).
[35] R. J. Nelmes, J. S. Loveday, T. Strässle, C. L. Bull, M. Guthrie, G. Hamel, and S. Klotz, Nat. Phys. **2**, 414 (2006).
[36] H. Li, M. Ladd-Parada, A. Karina, F. Dallari, M. Reiser, F. Perakis, N. N. Striker, M. Sprung, F. Westermeier, G. Grubel *et al.*, J. Phys. Chem. Lett. **14**, 10999 (2023).
[37] T. Loerting, W. Schustereder, K. Winkel, C. G. Salzmann, I. Kohl, and E. Mayer, Phys. Rev. Lett. **96**, 025702 (2006).
[38] D. Mariedahl, F. Perakis, A. Spah, H. Pathak, K. H. Kim, G. Camisasca, D. Schlesinger, C. Benmore, L. G. M. Pettersson, A. Nilsson, and K. Amann-Winkel, J. Phys. Chem. B **122**, 7616 (2018).
[39] P. H. Handle and T. Loerting, J. Chem. Phys. **148**, 124508 (2018).
[40] M. Ladd-Parada, K. Amann-Winkel, K. H. Kim, A. Spah, F. Perakis, H. Pathak, C. Yang, D. Mariedahl, T. Eklund, T. J. Lane *et al.*, J. Phys. Chem. B **126**, 2299 (2022).
[41] K. Winkel, M. S. Elsaesser, E. Mayer, and T. Loerting, J. Chem. Phys. **128**, 044510 (2008).
[42] F. Perakis, K. Amann-Winkel, F. Lehmkühler, M. Sprung, D. Mariedahl, J. A. Sellberg, H. Pathak, A. Späh, F. Cavalca, D. Schlesinger *et al.*, Proc. Natl. Acad. Sci. U. S. A. **114**, 8193 (2017).
[43] S. Lemke, P. H. Handle, L. J. Plaga, J. N. Stern, M. Seidl, V. Fuentes-Landete, K. Amann-Winkel, K. W. Köster, C. Gainaru, T. Loerting, and R. Böhmer, J. Chem. Phys. **147**, 034506 (2017).
[44] A. Eltareb, G. E. Lopez, and N. Giovambattista, Sci. Rep. **12**(1), 6004 (2022).
[45] M. A. González, C. Valeriani, F. Caupin, and J. L. Abascal, J. Chem. Phys. **145**, 054505 (2016).
[46] A. Eltareb, G. E. Lopez, and N. Giovambattista, J. Chem. Phys. **160**, 154510 (2024).
[47] P. H. Poole, F. Sciortino, U. Essmann, and H. E. Stanley, Nature **360**, 324 (1992).
[48] P. H. Poole, R. K. Bowles, I. Saika-Voivod, and F. Sciortino, J. Chem. Phys. **138**, 034505 (2013).
[49] F. Sciortino, E. La Nave, and P. Tartaglia, Phys. Rev. Lett. **91**, 155701 (2003).
[50] T. E. Gartner, L. Zhang, P. M. Piaggi, R. Car, A. Z. Panagiotopoulos, and P. G. Debenedetti, Proc. Natl. Acad. Sci. U. S. A. **117**, 26040 (2020).
[51] T. E. Gartner III, P. M. Piaggi, R. Car, A. Z. Panagiotopoulos, and P. G. Debenedetti, Phys. Rev. Lett. **129**, 255702 (2022).
[52] P. G. Debenedetti, F. Sciortino, and G. H. Zerze, Science **369**, 289 (2020).
[53] D. Dhabal, R. Kumar, and V. Molinero, Proc. Natl. Acad. Sci. U. S. A. **121**, e2322853121 (2024).
[54] F. Sciortino, T. E. Gartner, and P. G. Debenedetti, J. Chem. Phys. **160**, 104501 (2024).
[55] J. Weis, F. Sciortino, A. Z. Panagiotopoulos, and P. G. Debenedetti, J. Chem. Phys. **157**, 024502 (2022).
[56] K. H. Kim, A. Späh, H. Pathak, F. Perakis, D. Mariedahl, K. Amann-Winkel, J. A. Sellberg, J. H. Lee, S. Kim, J. Park *et al.*, Science **358**, 1589 (2017).
[57] H. Pathak, A. Späh, N. Esmaeildoost, J. A. Sellberg, K. H. Kim, F. Perakis, K. Amann-Winkel, M. Ladd-Parada, J. Koliyadu, T. J. Lane *et al.*, Proc. Natl. Acad. Sci. U. S. A. **118**, e2018379118 (2021).
[58] A. Späh, H. Pathak, K. H. Kim, F. Perakis, D. Mariedahl, K. Amann-Winkel, J. A. Sellberg, J. H. Lee, S. Kim, J. Park *et al.*, Phys. Chem. Chem. Phys. **21**, 26 (2019).
[59] K. Amann-Winkel, C. Gainaru, P. H. Handle, M. Seidl, H. Nelson, R. Bohmer, and T. Loerting, Proc. Natl. Acad. Sci. U. S. A. **110**, 17720 (2013).
[60] R. S. Singh, J. W. Biddle, P. G. Debenedetti, and M. A. Anisimov, J. Chem. Phys. **144**, 144504 (2016).
[61] V. Holten, J. C. Palmer, P. H. Poole, P. G. Debenedetti, and M. A. Anisimov, J. Chem. Phys. **140**, 104502 (2014).

[62]V. Holten and M. Anisimov, Sci. Rep. **2**(1), 713 (2012).
[63]V. Holten, C. Bertrand, M. Anisimov, and J. Sengers, J. Chem. Phys. **136**, 094507 (2012).
[64]J. W. Biddle, R. S. Singh, E. M. Sparano, F. Ricci, M. A. González, C. Valeriani, J. L. Abascal, P. G. Debenedetti, M. A. Anisimov, and F. Caupin, J. Chem. Phys. **146**, 034502 (2017).
[65]Z. Yu, R. Shi, and H. Tanaka, J. Phys. Chem. B **127**, 3452 (2023).
[66]J. Chiu, F. W. Starr, and N. Giovambattista, J. Chem. Phys. **139**, 184504 (2013).
[67]J. Chiu, F. W. Starr, and N. Giovambattista, J. Chem. Phys. **140**, 114504 (2014).
[68]N. Giovambattista, F. Sciortino, F. W. Starr, and P. H. Poole, J. Chem. Phys. **145**, 224501 (2016).
[69]P. H. Poole, U. Essmann, F. Sciortino, and H. E. Stanley, Phys. Rev. E **48**, 4605 (1993).
[70]N. Giovambattista and P. H. Poole, J. Non-Cryst. **11**, 100067 (2021).
[71]N. Giovambattista, H. E. Stanley, and F. Sciortino, Phys. Rev. E **72**, 031510 (2005).
[72]J. Wong, D. A. Jahn, and N. Giovambattista, J. Chem. Phys. **143**, 074501 (2015).
[73]J. Engstler and N. Giovambattista, J. Chem. Phys. **147**, 074505 (2017).
[74]A. Eltareb, G. E. Lopez, and N. Giovambattista, Phys. Chem. Chem. Phys. **23**, 19402 (2021).
[75]P. H. Handle, F. Sciortino, and N. Giovambattista, J. Chem. Phys. **150**, 244506 (2019).
[76]A. Eltareb, G. E. Lopez, and N. Giovambattista, Commun. Chem. **7**, 36 (2024).
[77]D. Dhabal and V. Molinero, J. Phys. Chem. B **127**, 2847 (2023).
[78]I. de Almeida Ribeiro, D. Dhabal, R. Kumar, S. Banik, S. Sankaranarayanan, and V. Molinero, Proc. Natl. Acad. Sci U. S. A. **121**(48), e2414444121 (2024).
[79]M. Tuckerman, *Statistical Mechanics: Theory and Molecular Simulation* (Oxford University Press, 2010).
[80]A. Eltareb, G. E. Lopez, and N. Giovambattista, J. Phys. Chem. B **127**, 4633 (2023).
[81]B. Pamuk, J. M. Soler, R. Ramírez, C. Herrero, P. Stephens, P. Allen, and M.-V. Fernández-Serra, Phys. Rev. Lett. **108**, 193003 (2012).
[82]C. P. Herrero and R. Ramírez, J. Chem. Phys. **134**, 094510 (2011).
[83]K. Komatsu, T. Hattori, S. Klotz, S. Machida, K. Yamashita, H. Ito, H. Kobayashi, T. Irifune, T. Shinmei, A. Sano-Furukawa, and H. Kagi, Nat. Commun. **15**, 5100 (2024).
[84]T. Meier, S. Petitgirard, S. Khandarkhaeva, and L. Dubrovinsky, Nat. Commun. **9**, 2766 (2018).
[85]S. Habershon, T. E. Markland, and D. E. Manolopoulos, J. Chem. Phys. **131**, 024501 (2009).
[86]A. Eltareb, G. E. Lopez, and N. Giovambattista, Phys. Chem. Chem. Phys. **23**, 6914 (2021).
[87]R. Ramírez and C. Herrero, Phys. Rev. B **84**, 064130 (2011).
[88]R. Ramírez, N. Neuerburg, M.-V. Fernandez-Serra, and C. Herrero, J. Chem. Phys. **137**, 044502 (2012).
[89]J. Bachler, J. Giebelmann, K. Amann-Winkel, and T. Loerting, J. Chem. Phys. **157**, 064502 (2022).
[90]G. Ramesh, V. Mahajan, D. Koner, and R. S. Singh, J. Chem. Phys. **160**, 194501 (2024).
[91]A. Garkul and V. Stegailov, Sci. Rep. **12**, 13325 (2022).
[92]F. Martelli, F. Leoni, F. Sciortino, and J. Russo, J. Chem. Phys. **153**, 104503 (2020).
[93]M. Ceriotti, M. Parrinello, T. E. Markland, and D. E. Manolopoulos, J. Chem. Phys. **133**, 124104 (2010).
[94]J. Åqvist, P. Wennerström, M. Nervall, S. Bjelic, and B. O. Brandsdal, Chem. Phys. Lett. **384**, 288 (2004).
[95]K.-H. Chow and D. M. Ferguson, Comput. Phys. Commun. **91**, 283 (1995).
[96]I. G. Tironi, R. Sperb, P. E. Smith, and W. F. van Gunsteren, J. Chem. Phys. **102**, 5451 (1995).
[97]P. Eastman, M. S. Friedrichs, J. D. Chodera, R. J. Radmer, C. M. Bruns, J. P. Ku, K. A. Beauchamp, T. J. Lane, L.-P. Wang, D. Shukla *et al.*, J. Chem. Theory Comput. **9**, 461 (2013).
[98]A. Eltareb, Y. Zhou, G. E. Lopez, and N. Giovambattista, Commun. Chem. **7**, 289 (2024).
[99]K. Röttger, A. Endriss, J. Ihringer, S. Doyle, and W. Kuhs, Acta Crystallogr., Sect. B:Struct. Sci. **50**, 644 (1994).
[100]D. T. Buckingham, J. Neumeier, S. H. Masunaga, and Y.-K. Yu, Phys. Rev. Lett. **121**, 185505 (2018).
[101]H. Tanaka, J. Mol. Liq. **90**, 323 (2001).
[102]A. Luzar and D. Chandler, Phys. Rev. Lett. **76**, 928 (1996).
[103]A. Karina, T. Eklund, C. M. Tonauer, H. Li, T. Loerting, and K. Amann-Winkel, J. Phys. Chem. Lett. **13**, 7965 (2022).
[104]M. L. Berrens, A. Kundu, M. F. Calegari Andrade, T. A. Pham, G. Galli, and D. Donadio, J. Phys. Chem. Lett. **15**, 6818 (2024).
[105]M. Ceriotti, W. Fang, P. G. Kusalik, R. H. McKenzie, A. Michaelides, M. A. Morales, and T. E. Markland, Chem. Rev. **116**, 7529 (2016).
[106]R. H. McKenzie, C. Bekker, B. Athokpam, and S. G. Ramesh, J. Chem. Phys. **140**, 174508 (2014).
[107]A. Eltareb, G. E. Lopez, and N. Giovambattista, J. Chem. Phys. **156**, 204502 (2022).
[108]Y. Liu, G. Sun, A. Eltareb, G. E. Lopez, N. Giovambattista, and L. Xu, Phys. Rev. Res. **2**, 013153 (2020).
[109]N. Giovambattista and G. E. Lopez, Phys. Rev. Res. **2**, 043441 (2020).
[110]N. Giovambattista, T. Loerting, B. R. Lukanov, and F. W. Starr, Sci. Rep. **2**(1), 390 (2012).
[111]C. P. Herrero and R. Ramírez, J. Chem. Phys. **137**, 104505 (2012).
[112]K. Winkel, M. Bauer, E. Mayer, M. Seidl, M. S. Elsaesser, and T. Loerting, J. Phys.: Condens. Matter **20**, 494212 (2008).
[113]J. Russo and H. Tanaka, Nat. Commun. **5**(1), 3556 (2014).
[114]J. Finney, A. Hallbrucker, I. Kohl, A. Soper, and D. Bowron, Phys. Rev. Lett. **88**, 225503 (2002).
[115]A. Narten, C.-G. Venkatesh, and S. Rice, J. Chem. Phys. **64**, 1106 (1976).
[116]B. Pamuk, P. Allen, and M.-V. Fernández-Serra, J. Phys. Chem. B **122**, 5694 (2018).
[117]C. P. Herrero and R. Ramírez, Mol. Phys. (published online 2024).
[118]O. Mishima, Nature **384**, 546 (1996).
[119]T. J. Boerner, S. Deems, T. R. Furlani, S. L. Knuth, and J. Towns, in *Practice and Experience in Advanced Research Computing (PEARC'23), Portland, OR, USA* (ACM, New York, 2023), p. 4.